

ESTIMATION OF TURBULENT VISCOSITY AND DIFFUSIVITY IN ADJOINT RECOVERY OF ATMOSPHERIC BOUNDARY LAYER FLOW STRUCTURES*

TIANFENG CHAI[†] AND CHING-LONG LIN[†]

Abstract. A method to estimate turbulent eddy viscosity and thermal diffusivity during a four-dimensional variational data assimilation process is proposed to retrieve microscale atmospheric boundary layer flow structures. Vertical profiles of eddy viscosity and thermal diffusivity are treated as part of control variables in data assimilation to circumvent subgrid-scale modeling and laborious parameter tuning. These profiles are optimal in that they lead to best data fitting. The proposed method is validated and evaluated by conducting two sets of identical twin experiments. In one set, profiles of viscosity and/or diffusivity are assumed to be the only control variables and are recovered accurately. The other set aims to recover profiles as well as initial velocity and temperature fields. The proposed method accurately recovers eddy viscosity. The optimized parameters also improve retrieved velocity and temperature data quality compared to approaches using prespecified parameters. Issues of initial guess, observational errors, and control variable rescaling are examined.

Key words. adjoint method, data assimilation, atmospheric boundary layer, parameter estimation

AMS subject classifications. 49N45, 76D05, 86N10

PII. S1540345902411414

1. Introduction. The four-dimensional variational data assimilation (4D-Var) technique is based on variational analysis and optimal control theory to recover complete and dynamically consistent data sets by minimizing the difference between limited observations and corresponding model predictions. Intensive research has been conducted on mesoscale atmospheric flows using models of increasing complexity and dimension [28, 20, 16, 37, 32, 26, 27]. Control variables of data assimilation under a strict mathematical framework include initial conditions, boundary conditions, and all the parameters involved in the physical model, such as eddy viscosity and thermal diffusivity [8]. Due to the complex nature of atmospheric and oceanic systems and the consequent unrealistic demand on memory and computation time, the general formulations of 4D-Var are difficult to apply. In most 4D-Var for mesoscale atmospheric flows, control variables include the initial flow field only. Eddy viscosity and thermal diffusivity are assumed constant throughout the computational domain [24, 25]. This simplification is likely to introduce large errors into the atmospheric boundary layer (ABL) flow where the vertical variation of turbulence intensity is significant.

Although the recovery of turbulent viscosity from atmospheric data has never been reported, estimations of turbulent viscosity profiles from oceanic observations have been attempted to avoid the laborious task of tuning parameters by trial and error. Yu and O'Brien [33] used a simple oceanic Ekman layer model to assimilate meteorological and oceanographic observations. They found that the variational assimilation technique can reveal the vertical distribution of eddy viscosity. Panchang and Richardson [19] estimated eddy viscosity vertical profiles for a three-dimensional

*Received by the editors July 16, 2002; accepted for publication (in revised form) March 17, 2003; published electronically May 1, 2003. This work was supported by National Science Foundation ATM grant 9874925 and monitored by Dr. Roddy R. Rogers.
<http://www.siam.org/journals/mms/1-2/41141.html>

[†]Department of Mechanical and Industrial Engineering, IIHR-Hydrosience and Engineering, University of Iowa, Iowa City, IA 52242-1527 (tianfeng-chai@uiowa.edu, ching-long-lin@uiowa.edu).

(3D) coastal circulation model by assimilating observational data using an adjoint method. A detailed survey of the parameter estimation in meteorology and oceanography was given by Navon [17].

Recently, Zhu and Navon [35] conducted experiments with the full-physics adjoint of the FSU Global Spectral Model to study the effect of the parameter estimation with the data assimilation approach. They carried out 4D-Var with both initial conditions and three parameters as control variables. The parameters were the biharmonic horizontal diffusion coefficient, the Asselin filter coefficient, and the ratio of the transfer coefficient of moisture to the transfer coefficient of sensible heat. They observed a positive impact due to retrieved optimal parameter values. However, the parameters studied in their paper were assumed to be constants in time and space. Recent work by Leredde, Devenon, and DeKeyser [9] showed that data assimilation can estimate a time- and space-dependent turbulent viscosity using a 3D oceanic circulation model. In their study, eddy viscosity was the only control variable. The synthetic observations were obtained using a k - ε model (k , turbulent kinetic energy; ε , turbulent dissipation rate). Their results showed that eddy viscosity can be recovered by data assimilation without a turbulence model.

Advances in lidar systems (e.g., [3, 6]) make the ABL data of higher spatial and temporal resolutions available. Assimilation of lidar observational data has the potential to reveal microscale turbulence structures present in the ABL and their interactions with mesoscale structures. In the ABL flows, vertical scales are no longer much smaller than lateral scales, as they are in the mesoscale flows. Vertical variation of turbulence intensity must be accounted for to properly retrieve the ABL flows under varying stability conditions.

Lin, Chai, and Sun [10] formulated eddy viscosity and thermal diffusivity as functions of height in the identical twin experiments (ITEs) to recover convective boundary layer (CBL) flow structures through 4D-Var. These experiments used the 4D-Var prediction model to generate synthetic observations. Eddy viscosity and thermal diffusivity profiles were prescribed prior to data assimilation. Approximating such flow parameters with little wind and temperature data is difficult, if not impossible. In contrast with subgrid scale (SGS) parameterizations in large-eddy simulation (LES), these parameters may be derived from field observations through the data assimilation technique to eliminate parameterization errors. In this study, we treat vertical profiles of eddy viscosity and thermal diffusivity, as well as the 3D initial velocity and temperature fields as control variables in 4D-Var.

There are two main objectives in the current study. The first is to determine whether eddy viscosity and thermal diffusivity can be extracted from the ABL observations using the adjoint method. This is achieved by treating eddy viscosity and/or thermal diffusivity as the only control variables with given initial 3D velocity and temperature fields. The second objective is to ascertain whether adding eddy viscosity and thermal diffusivity as control variables improves velocity and temperature retrieval more than arbitrarily specified profiles. Issues of initial guess, observational errors, and control variable rescaling are also investigated.

The paper is organized as follows. Methodology is briefly explained in section 2. In section 3, the proposed method is validated using ITEs with given initial velocity and temperature fields. In section 4, profiles of eddy viscosity and thermal diffusion, and initial velocity and temperature fields are retrieved by 4D-Var. Concluding remarks are stated in section 5.

2. Parameter optimization using the adjoint method.

2.1. Prediction model. The current 4D-Var system is based on the one presented in [10] and consists of three parts: prediction model, adjoint model, and minimization. In this system, with a first guess of control variables, the prediction model is integrated forward in time. Computed velocity and temperature fields are subsequently used for backward integration of adjoint equations forced with data misfit to obtain gradient information for control variables. The gradient information then is supplied to a minimization scheme that updates control variables for optimal data fit.

The governing equations of the prediction model include the continuity equation (2.1), the momentum equations (2.2)–(2.4), and the energy equation (2.5) for incompressible flow with Boussinesq approximation:

$$(2.1) \quad \frac{\partial U}{\partial x} + \frac{\partial V}{\partial y} + \frac{\partial W}{\partial z} = 0,$$

$$(2.2) \quad \begin{aligned} & \frac{\partial U}{\partial t} + U \frac{\partial U}{\partial x} + V \frac{\partial U}{\partial y} + W \frac{\partial U}{\partial z} \\ &= -\frac{1}{\rho_o} \frac{\partial P}{\partial x} + \nu(z) \left(\frac{\partial^2 U}{\partial x^2} + \frac{\partial^2 U}{\partial y^2} \right) + \frac{\partial}{\partial z} \left(\nu(z) \frac{\partial U}{\partial z} \right), \end{aligned}$$

$$(2.3) \quad \begin{aligned} & \frac{\partial V}{\partial t} + U \frac{\partial V}{\partial x} + V \frac{\partial V}{\partial y} + W \frac{\partial V}{\partial z} \\ &= -\frac{1}{\rho_o} \frac{\partial P}{\partial y} + \nu(z) \left(\frac{\partial^2 V}{\partial x^2} + \frac{\partial^2 V}{\partial y^2} \right) + \frac{\partial}{\partial z} \left(\nu(z) \frac{\partial V}{\partial z} \right), \end{aligned}$$

$$(2.4) \quad \begin{aligned} & \frac{\partial W}{\partial t} + U \frac{\partial W}{\partial x} + V \frac{\partial W}{\partial y} + W \frac{\partial W}{\partial z} \\ &= -\frac{1}{\rho_o} \frac{\partial P}{\partial z} - \frac{g\theta}{\Theta_o} + \nu(z) \left(\frac{\partial^2 W}{\partial x^2} + \frac{\partial^2 W}{\partial y^2} \right) + \frac{\partial}{\partial z} \left(\nu(z) \frac{\partial W}{\partial z} \right), \end{aligned}$$

$$(2.5) \quad \begin{aligned} & \frac{\partial \theta}{\partial t} + U \frac{\partial \theta}{\partial x} + V \frac{\partial \theta}{\partial y} + W \frac{\partial \theta}{\partial z} + W \frac{d\Theta(z)}{dz} \\ &= \kappa(z) \left(\frac{\partial^2 \theta}{\partial x^2} + \frac{\partial^2 \theta}{\partial y^2} \right) + \frac{\partial}{\partial z} \left(\kappa(z) \frac{\partial(\Theta(z) + \theta)}{\partial z} \right), \end{aligned}$$

where U , V , and W are velocity components in the x -, y -, and z -directions. θ , $\Theta(z)$, and Θ_o are fluctuating, background, and reference virtual potential temperatures, respectively. g is gravity acceleration. P is pressure. In these equations, Θ_o and ρ_o are constants. Unless otherwise noted, all dependent variables are functions of x , y , z , and t . $(0, L_x) \times (0, L_y) \times (0, L_z) \times (0, T)$ defines the four-dimensional (4D) computational domain. Lowercase variables denote fluctuating variable components.

Eddy viscosity $\nu(z)$ and thermal diffusivity $\kappa(z)$ are assumed to be height-dependent. They could be 4D variables. Compared with recovering initial 3D wind and temperature data, however, retrieving 4D ν and κ substantially increases the number of control variables, and subsequently requires many more observations for an optimum solution. With today's lidar and computer technology, this is very difficult, if not impossible.

In the ITEs, Dirichlet boundary conditions are applied laterally. At the top boundary, the gradient-free boundary condition is implemented. The Monin–Obukhov similarity theory is applied at the first vertical grid level immediately above the surface (see [10]). Dependent variables are arranged on a staggered, orthogonal grid. The second-order finite volume method is applied for spatial differencing. The second-order Adam–Bashforth method is used for the time advancement of dependent variables. Mass conservation is enforced by solving a pressure–Poisson equation derived from continuity equations (2.1) and momentum equations (2.2)–(2.4).

2.2. Adjoint equations.

2.2.1. Formulation of 4D-Var. We first relate our 4D-Var method to the optimal control theory described by Talagrand and Courtier [28]. Assuming no large-scale pressure gradient, the initial pressure field is set to zero everywhere. Control system input ξ includes $\nu(z)$, $\kappa(z)$, and initial state variables except pressure:

$$(2.6) \quad \begin{aligned} \xi = & \xi(U(x, y, z, t=0), V(x, y, z, t=0), W(x, y, z, t=0), \\ & \theta(x, y, z, t=0), \nu(z), \kappa(z)). \end{aligned}$$

4D state variable ζ can be expressed as

$$(2.7) \quad \begin{aligned} \zeta = & \zeta(U(x, y, z, t), V(x, y, z, t), W(x, y, z, t), \\ & \theta(x, y, z, t), P(x, y, z, t)). \end{aligned}$$

With ξ available, state variables ζ can be obtained by time integration of (2.1)–(2.5). Problem output is a simple scalar function H , defined to measure the difference between model predictions and field observations:

$$(2.8) \quad H(\zeta) = \frac{1}{L_x L_y L_z T} \int_0^T \int_0^{L_z} \int_0^{L_y} \int_0^{L_x} \frac{(U_{rad} - U_{rad}^{obs})^2}{\sigma^2} dx dy dz dt,$$

where U_{rad}^{obs} denotes the radial velocity field observation and σ^2 is the observational variance. U_{rad} is radial velocity constructed from predicted velocity using the relationship

$$(2.9) \quad U_{rad} = \frac{U \cdot (x - x_o) + V \cdot (y - y_o) + W \cdot (z - z_o)}{r},$$

where $r = \sqrt{(x - x_o)^2 + (y - y_o)^2 + (z - z_o)^2}$ and (x_o, y_o, z_o) denotes the lidar coordinates. Output function $H(\zeta)$, also known as the cost function, is minimized with the optimization algorithm. In the general formulation of the cost function [17, 36], the difference between model parameters and estimated parameters is also added to the cost function. Absence of such a term in (2.8) is due to the difficulty of estimating eddy viscosity and thermal diffusivity in the ABL flow.

We then focus on derivation of the adjoint equations for the control variables $\nu(z)$ and $\kappa(z)$, which are new additions to the system. In the next section, a one-dimensional (1D) model diffusion equation is used to demonstrate the procedure.

2.2.2. 1D model diffusion equation. Let us consider the following 1D model diffusion equation:

$$(2.10) \quad \frac{\partial u}{\partial t} = \frac{\partial}{\partial x} \left(\nu(x) \frac{\partial u}{\partial x} \right),$$

where $u = u(x, t)$. The initial condition and parameter $\nu(x)$ are taken as control variables. Control and state variables are $\xi(u(x, t = 0), \nu(x))$ and $\zeta(u(x, t))$, respectively. The cost function is defined as

$$(2.11) \quad H = \frac{1}{LT} \int_0^T \int_0^L \frac{(u - u^{obs})^2}{\sigma^2} dx dt.$$

To derive adjoint equations, we introduce the Lagrange multiplier of $\lambda_u(x, t)$, also known as adjoint variables, and write the new cost function as

$$(2.12) \quad \begin{aligned} H = & \frac{1}{LT} \int_0^T \int_0^L \frac{(u - u^{obs})^2}{\sigma^2} dx dt \\ & + \frac{1}{LT} \int_0^T \int_0^L \lambda_u \left[\frac{\partial u}{\partial t} - \frac{\partial}{\partial x} \left(\nu(x) \frac{\partial u}{\partial x} \right) \right] dx dt. \end{aligned}$$

In this way, the optimization is transformed into an unconstrained minimization problem. The variation of (2.12) yields

$$(2.13) \quad \begin{aligned} \delta H = & \frac{1}{LT} \int_0^T \int_0^L \frac{2(u - u^{obs})}{\sigma^2} \delta u dx dt \\ & + \frac{1}{LT} \int_0^T \int_0^L \delta \lambda_u \left[\frac{\partial u}{\partial t} - \frac{\partial}{\partial x} \left(\nu(x) \frac{\partial u}{\partial x} \right) \right] dx dt \\ & + \frac{1}{LT} \int_0^T \int_0^L \lambda_u \left[\frac{\partial \delta u}{\partial t} - \frac{\partial}{\partial x} \left(\delta \nu(x) \frac{\partial u}{\partial x} + \nu(x) \frac{\partial \delta u}{\partial x} \right) \right] dx dt. \end{aligned}$$

Integration of (2.13) by parts yields

$$(2.14) \quad \begin{aligned} \delta H = & \frac{1}{LT} \int_0^T \int_0^L \delta u \left[\frac{2(u - u^{obs})}{\sigma^2} - \frac{\partial \lambda_u}{\partial t} - \frac{\partial}{\partial x} \left(\nu(x) \frac{\partial \lambda_u}{\partial x} \right) \right] dx dt \\ & + \frac{1}{LT} \int_0^T \int_0^L \delta \lambda_u \left[\frac{\partial u}{\partial t} - \frac{\partial}{\partial x} \left(\nu(x) \frac{\partial u}{\partial x} \right) \right] dx dt \\ & + \frac{1}{LT} \int_0^T \int_0^L \delta \nu(x) \frac{\partial u}{\partial x} \frac{\partial \lambda_u}{\partial x} dx dt \\ & + \frac{1}{LT} \int_0^L (\lambda_u \delta u)|_{t=T} dx \\ & - \frac{1}{LT} \int_0^L (\lambda_u \delta u)|_{t=0} dx \\ & + \frac{1}{LT} \int_0^T \left[-\lambda_u \delta \nu(x) \frac{\partial u}{\partial x} - \lambda_u \nu(x) \frac{\partial \delta u}{\partial x} + \frac{\partial \lambda_u}{\partial x} \nu(x) \delta u \right]_0^L dt. \end{aligned}$$

The second term on the right-hand side (RHS) vanishes as the state variable satisfies governing equation (2.10). Assigning “initial” condition $\lambda_u = 0$ at $t = T$, the fourth RHS term disappears. The last term vanishes by choosing appropriate boundary conditions for λ_u . For instance, use of the Dirichlet boundary condition for u results in $\lambda_u = 0$ at $x = 0$ and $x = L$. The adjoint equation is obtained with the integrand in the first term set to zero:

$$(2.15) \quad \frac{\partial \lambda_u}{\partial t} = -\frac{\partial}{\partial x} \left(\nu(x) \frac{\partial \lambda_u}{\partial x} \right) + \frac{2(u - u^{obs})}{\sigma^2}.$$

With the above adjoint equation satisfied, (2.14) reduces to

$$(2.16) \quad \begin{aligned} \delta H = & \frac{1}{LT} \int_0^T \int_0^L \delta \nu(x) \frac{\partial u}{\partial x} \frac{\partial \lambda_u}{\partial x} dx dt \\ & - \frac{1}{LT} \int_0^L \lambda_u(t=0) \delta u(t=0) dx. \end{aligned}$$

Cost function gradients with respect to the state variable at $t = 0$ and $\nu(x)$ can then be uniquely defined as

$$(2.17) \quad \nabla_{u(t=0)} H = -\lambda_u(t=0),$$

$$(2.18) \quad \nabla_{\nu(x)} H = \frac{1}{T} \int_0^T \frac{\partial u}{\partial x} \frac{\partial \lambda_u}{\partial x} dt.$$

The gradient shown in (2.17) is nothing but $-\lambda_u$ at the initial time. The value of λ_u is obtained by integrating adjoint equation (2.15) backward in time with the initial condition of $\lambda_u(t = T) = 0$. The gradient in (2.18) depends on the spatial derivatives of state and adjoint variables. No new variables are required to calculate this gradient. This feature makes the parameter retrieval very appealing. If viscosity depends on time and space, the gradient becomes a function of time and space shown below:

$$(2.19) \quad \nabla_{\nu(x,t)} H = \frac{\partial u}{\partial x} \frac{\partial \lambda_u}{\partial x}.$$

2.2.3. Adjoint equations and gradients in 4D-Var. We can follow the above derivation to find the adjoint equations for 4D-Var:

$$(2.20) \quad \begin{aligned} \frac{\partial \lambda_U}{\partial t} = & -2U \frac{\partial \lambda_U}{\partial x} - V \frac{\partial \lambda_U}{\partial y} - W \frac{\partial \lambda_U}{\partial z} - V \frac{\partial \lambda_V}{\partial x} - W \frac{\partial \lambda_W}{\partial x} - \theta \frac{\partial \lambda_\theta}{\partial x} \\ & + 2U \frac{\partial^2 \lambda_P}{\partial x \partial x} + 2V \frac{\partial^2 \lambda_P}{\partial y \partial x} + 2W \frac{\partial^2 \lambda_P}{\partial z \partial x} + \nu(z) \left(\frac{\partial^2 \lambda_U}{\partial x \partial x} + \frac{\partial^2 \lambda_U}{\partial y \partial y} \right) \\ & + \frac{\partial}{\partial z} \left(\nu(z) \frac{\partial \lambda_U}{\partial z} \right) + 2 \frac{(x - x_0)}{r} \frac{U_{rad} - U_{rad}^{obs}}{\sigma^2}, \end{aligned}$$

$$(2.21) \quad \begin{aligned} \frac{\partial \lambda_V}{\partial t} = & -U \frac{\partial \lambda_V}{\partial x} - 2V \frac{\partial \lambda_V}{\partial y} - W \frac{\partial \lambda_V}{\partial z} - U \frac{\partial \lambda_U}{\partial y} - W \frac{\partial \lambda_W}{\partial y} - \theta \frac{\partial \lambda_\theta}{\partial y} \\ & + 2V \frac{\partial^2 \lambda_P}{\partial x \partial y} + 2V \frac{\partial^2 \lambda_P}{\partial y \partial y} + 2W \frac{\partial^2 \lambda_P}{\partial z \partial y} + \nu(z) \left(\frac{\partial^2 \lambda_V}{\partial x \partial x} + \frac{\partial^2 \lambda_V}{\partial y \partial y} \right) \\ & + \frac{\partial}{\partial z} \left(\nu(z) \frac{\partial \lambda_V}{\partial z} \right) + 2 \frac{(y - y_0)}{r} \frac{U_{rad} - U_{rad}^{obs}}{\sigma^2}, \end{aligned}$$

$$(2.22) \quad \begin{aligned} \frac{\partial \lambda_W}{\partial t} = & -U \frac{\partial \lambda_W}{\partial x} - V \frac{\partial \lambda_W}{\partial y} - 2W \frac{\partial \lambda_W}{\partial z} - U \frac{\partial \lambda_U}{\partial z} - V \frac{\partial \lambda_V}{\partial z} - \theta \frac{\partial \lambda_\theta}{\partial z} \\ & + 2U \frac{\partial^2 \lambda_P}{\partial x \partial z} + 2V \frac{\partial^2 \lambda_P}{\partial y \partial z} + 2W \frac{\partial^2 \lambda_P}{\partial z \partial z} + \nu(z) \left(\frac{\partial^2 \lambda_W}{\partial x \partial x} + \frac{\partial^2 \lambda_W}{\partial y \partial y} \right) \\ & + \frac{\partial}{\partial z} \left(\nu(z) \frac{\partial \lambda_W}{\partial z} \right) + 2 \frac{(z - z_0)}{r} \frac{U_{rad} - U_{rad}^{obs}}{\sigma^2}, \end{aligned}$$

$$\frac{\partial \lambda_\theta}{\partial t} = -U \frac{\partial \lambda_\theta}{\partial x} - V \frac{\partial \lambda_\theta}{\partial y} - W \frac{\partial \lambda_\theta}{\partial z} + \frac{g}{\Theta_0} \lambda_W - \frac{g}{\Theta_0} \frac{\partial \lambda_P}{\partial z}$$

$$(2.23) \quad -\kappa(z) \left(\frac{\partial^2 \lambda_\theta}{\partial x \partial x} + \frac{\partial^2 \lambda_\theta}{\partial y \partial y} \right) - \frac{\partial}{\partial z} \left(\kappa(z) \frac{\partial \lambda_\theta}{\partial z} \right)$$

$$(2.24) \quad 0 = \frac{\partial^2 \lambda_P}{\partial x \partial x} + \frac{\partial^2 \lambda_P}{\partial y \partial y} + \frac{\partial^2 \lambda_P}{\partial z \partial z} - \frac{\partial \lambda_U}{\partial x} - \frac{\partial \lambda_V}{\partial y} - \frac{\partial \lambda_W}{\partial z}.$$

The cost function gradients with respect to the control variables are

$$(2.25) \quad \nabla_{U(t=0)} H = -\lambda_U(t=0),$$

$$(2.26) \quad \nabla_{V(t=0)} H = -\lambda_V(t=0),$$

$$(2.27) \quad \nabla_{W(t=0)} H = -\lambda_W(t=0),$$

$$(2.28) \quad \nabla_{\theta(t=0)} H = -\lambda_\theta(t=0),$$

$$(2.29) \quad \nabla_{\nu(z)} H = \frac{1}{L_x L_y T} \int_0^T \int_0^{L_y} \int_0^{L_x} \left(\frac{\partial \lambda_U}{\partial x} \frac{\partial U}{\partial x} + \frac{\partial \lambda_U}{\partial y} \frac{\partial U}{\partial y} + \frac{\partial \lambda_U}{\partial z} \frac{\partial U}{\partial z} + \frac{\partial \lambda_V}{\partial x} \frac{\partial V}{\partial x} + \frac{\partial \lambda_V}{\partial y} \frac{\partial V}{\partial y} + \frac{\partial \lambda_V}{\partial z} \frac{\partial V}{\partial z} + \frac{\partial \lambda_W}{\partial x} \frac{\partial W}{\partial x} + \frac{\partial \lambda_W}{\partial y} \frac{\partial W}{\partial y} + \frac{\partial \lambda_W}{\partial z} \frac{\partial W}{\partial z} \right) dx dy dt,$$

$$(2.30) \quad \nabla_{\kappa(z)} H = \frac{1}{L_x L_y T} \int_0^T \int_0^{L_y} \int_0^{L_x} \left(\frac{\partial \lambda_\theta}{\partial x} \frac{\partial \theta}{\partial x} + \frac{\partial \lambda_\theta}{\partial y} \frac{\partial \theta}{\partial y} + \frac{\partial \lambda_\theta}{\partial z} \frac{\partial \theta}{\partial z} \right) dx dy dt.$$

Addition of the parameters $\nu(z)$ and $\kappa(z)$ as control variables neither changes the appearance of the adjoint equations nor introduces new adjoint variables. This renders the parameter retrieval straightforward to implement in the existing 4D-Var model. To expand the parameters' degree of freedom to more than one dimension, such as t and z , the time integration in (2.29) and (2.30) should be omitted. One final note about the adjoint equation is that space and time discretizations of the prediction model and its adjoint model must be numerically consistent. To achieve this, the adjoint model has been derived from the discretized prediction equations.

2.3. Optimization method. With the gradients available via the adjoint model, we apply a quasi-Newton method to minimize the cost function by updating control variables. Due to the large number of control variables in 4D-Var, the limited memory BFGS (L-BFGS) method [12] is applied in the current study. The L-BFGS method is slightly different from the BFGS method in that it stores only m BFGS corrections to avoid using $\mathcal{O}(n^2)$ storage, where n represents the number of control variables. For this study, $m = 3$. The BFGS method is considered one of the best quasi-Newton formulae [18]. Although truncated Newton (TN) outperforms L-BFGS for quadratic and approximately quadratic problems, L-BFGS is suited for highly nonlinear problems, outperforming TN in most cases [15]. Zou et al. [38] demonstrated that L-BFGS performs better than the full-memory BFGS method, especially in terms of the total CPU time.

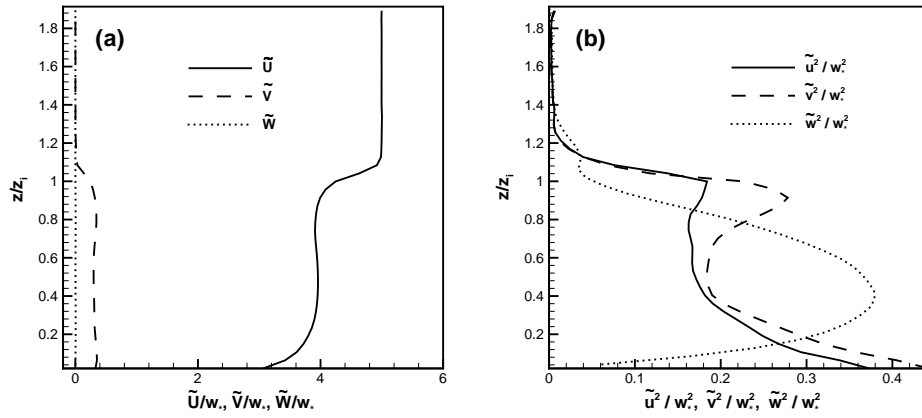


FIG. 1. Vertical distributions of (a) mean velocity and (b) normalized velocity variance. Symbol “ \sim ” denotes averaging over time and the x - y plane. w_* , the free-convection velocity scale, is 2.0 m/s.

3. Validation.

3.1. Numerical experiments. In the ITEs, synthetic observational data are generated by the 4D-Var prediction model. Although ITEs often generate overly optimistic results, they nevertheless serve well for validation because exact data are available for retrieval quality assessment. A grid size of $N_x \times N_y \times N_z = 48 \times 48 \times 45$ is used on a computational domain of $5 \times 5 \times 1.875$ km³ with a spatial resolution of 104.2 m in the horizontal direction and 41.7 m in the vertical direction. The assimilation time window is chosen as 300 sec, and the time step is 5 sec. The size of the computational domain is comparable to that of a typical high resolution Doppler lidar scan volume, and the assimilation time window allows three complete volume scans [1]. In the ITEs, the simulated CBL flow is driven by a 10 m/s geostrophic wind and a temperature flux $Q_s = 0.24$ K · m/s (K, Kelvin temperature scale). A capping inversion layer is imposed at about $z_i = 980$ m (average CBL height). The roughness height z_o is 0.16 m. The stability parameter $-z_i/L$ is about 15, where L is the Monin–Obukhov length. The convective scaling velocity w_* [21] is 2 m/s. The convective temperature scale $\theta_*(\equiv Q_s/w_*)$ is 0.12 K.

To generate meaningful observational data from the 4D-Var prediction model for the following ITEs, initial and boundary conditions along with viscosity and diffusivity profiles are needed. Those are obtained through the LES code developed by Moeng [13] and Sullivan, McWilliams, and Moeng [22]. Before capturing the required information in a 5-minute period, the LES code is first carried out for a long period of time in order to have a well-resolved turbulent flow field. There are 13 3D instantaneous data sets recorded with a time interval of 25 sec. The profiles of mean velocity and velocity variance during the 5-minute period are displayed in Figure 1. The maximum value of normalized vertical velocity variance is close to 0.4. It agrees with the field data of CBL measured by Lenschow, Wyngaard, and Pennell [7].

Assuming the lidar location at $(x_o, y_o, z_o) = (0.0, 0.0, 20.8)$ m, we calculate the radial velocity for every grid point using (2.9) with the synthetic “exact” velocity data. These radial velocity data are provided as the 4D-Var input parameters. Figure 2

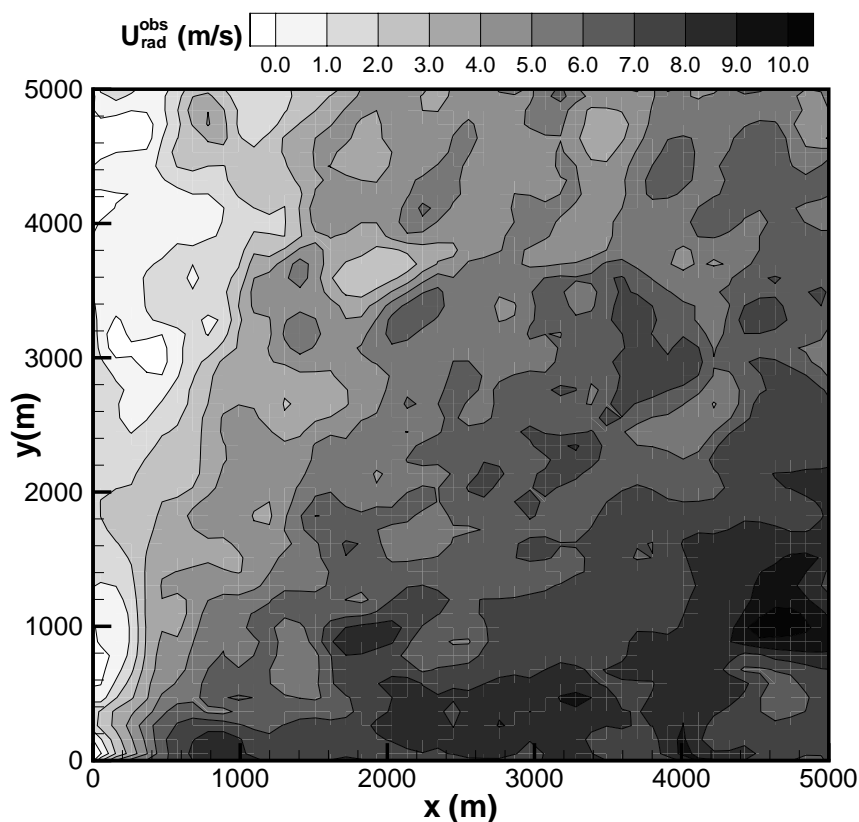


FIG. 2. Contours of U_{rad}^{obs} at $t = 150$ sec, $z = 480.0$ m from observation set B.

shows a typical radial velocity contour plot at a selected height. Not much information is obtained from the plot. Besides radial velocity, the profile of mean virtual potential temperature, shown in Figure 1(a), is supplied to the 4D-Var model. Variance σ^2 in (2.8) acts as the inverse of the weight factor for each available radial velocity. In the study, $1/\sigma^2$ is set at $1 \text{ s}^2/\text{m}^2$ to give equal weight to each observation. The correctness of the gradient calculated from (2.29) and (2.30) is verified using the same approach as [23, 34].

3.2. Recovery of eddy viscosity and thermal diffusivity. In this section, we consider three sets of the ITEs. The first set takes eddy viscosity as the only control variable. Another set treats thermal diffusivity as the control variable. The third set has both eddy viscosity and thermal diffusivity as control variables. At this stage, the synthetic observational data are free of error. Although the available radial velocity contains no temperature information, these experiments permit us to recover thermal diffusivity because of the coupling between momentum and energy equations. The issues about the retrieval sensitivity to initial guess and scaling effect are also discussed. To address these issues, three different observation sets are generated. Descriptions of the experiments are given in Table 1. Generation of observation set A (section 3.1) uses viscosity and diffusivity profiles displayed in Figures 3(a) and

TABLE 1

Descriptions of ITEs presented in section 3. Observation sets A, B, and C are generated using $\nu(z)$ profiles shown in Figures 3(a), 3(b), and 3(c), respectively. The $\kappa(z)$ profile in Figure 4 is used to generate observation set A. $\kappa(z)$ profiles used to generate observation sets B and C are obtained using (3.3), with $Pr = 0.4$. Cases 5 and 6 use different initial guesses for $\nu(z)$ and $\kappa(z)$.

Case	Control variables	Observation set	Iterations conducted
1	$\nu(z)$	A	18
2	$\nu(z)$	B	13
3	$\nu(z)$	C	13
4	$\kappa(z)$	B	45
5	$\nu(z), \kappa(z)$	B	50
6	$\nu(z), \kappa(z)$	B	50
7	$\nu(z), \kappa(z)/2$	B	50

4, respectively. They are obtained by averaging at each height the ν and κ values calculated in the LES code by

$$(3.1) \quad \nu = 0.1le^{1/2},$$

$$(3.2) \quad \kappa = \left(1 + \frac{2l}{\Delta}\right) \nu,$$

where e stands for the SGS turbulent energy (obtained from a prognostic SGS turbulent kinetic energy equation; see [13, 22]), l is the mixing length, and Δ is the averaged grid spacing.

Two other eddy viscosity profiles in Figures 3(b) and 3(c) emulate two different conditions. For observation set B, SGS turbulence intensity has a maximum value at some distance above the ground, with $\nu(z)$ following the sinusoidal function. Observation set C is generated using a linear distribution of $\nu(z)$, which has a maximum value on the ground. Thermal diffusivity profiles used to generate these two observation sets are approximated by

$$(3.3) \quad \kappa(z) = Pr^{-1} \cdot \nu(z),$$

where the turbulent Prandtl number $Pr = 0.4$. With these profiles specified and initial velocity and temperature fields given by the LES code, the observations for the ITEs are generated using the prediction model.

3.2.1. Eddy viscosity recovery. For cases 1, 2, and 3 in Table 1, which use observation sets A, B, and C, initial velocity and temperature fields and thermal diffusivity profile are provided. Figure 3(d) shows the initial guess for profile $\nu(z)$, which is used for all the cases in Table 1 unless otherwise noted. This initial guess is based on the fact that turbulent activity diminishes above the capping layer. The sensitivity of retrieval quality to the initial guess is discussed later. The following convergence criterion is applied to the minimization procedure:

$$(3.4) \quad \frac{\|\nabla_{\xi} H\|}{\|\nabla_{\xi} H\|_{Iter=0}} < 0.001.$$

Here the gradient calculated from the initial guess, denoted by the subscript $Iter = 0$, is used as a reference value. The gradient norm $\|\nabla_{\xi} H\|$ is defined as

$$(3.5) \quad \|\nabla_{\xi} H\| = \sqrt{\frac{\sum_1^N \nabla_{\xi} H_i^2}{N}},$$

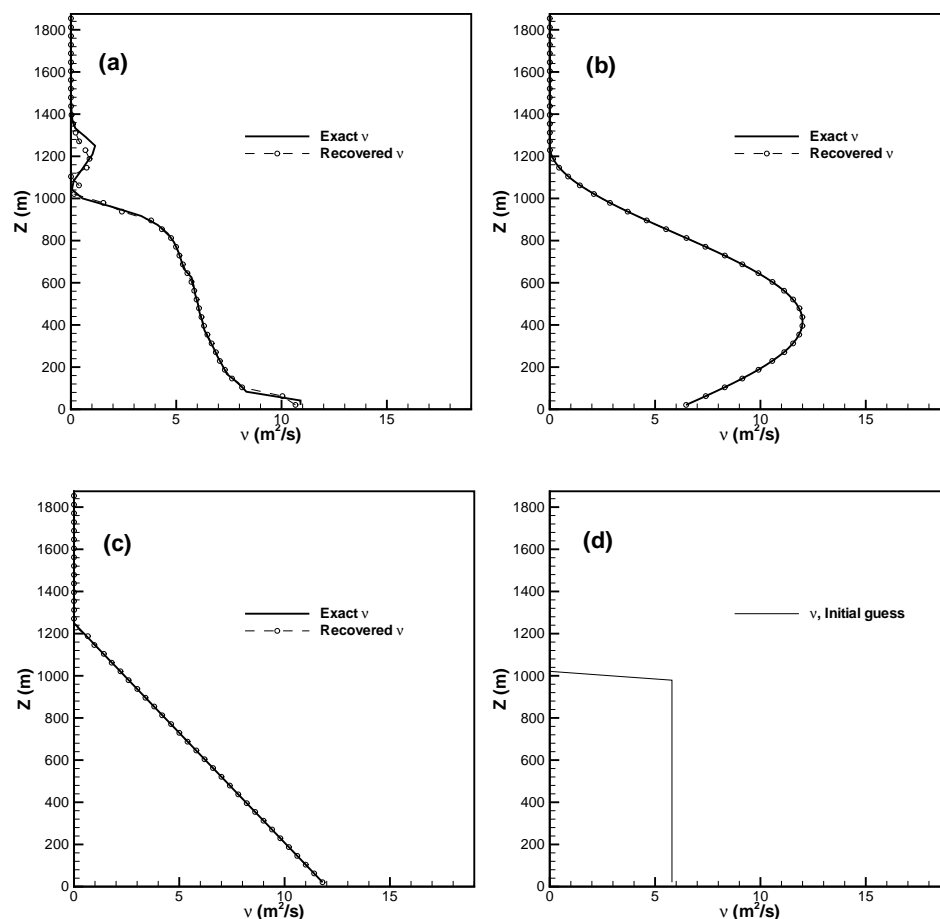


FIG. 3. Exact and recovered eddy viscosity profiles for observation sets (a) A, (b) B, and (c) C. Exact ν profiles are those used to generate observation sets. The initial guess for the eddy viscosity profile for the three cases is displayed in (d).

where N is the dimension of the control variable vector ξ . The optimization procedure is terminated if the convergence criterion is not met within 50 iterations. Since the number of control variables is very small ($N_z = 45$ for one profile or 90 for two profiles), the optimal solution can usually be obtained within 50 iterations. The iteration number is given in Table 1. Figures 3(a), 3(b), and 3(c) display recovered eddy viscosity profiles for cases 1, 2, and 3, respectively. They collapse nearly with the exact profiles that are used to generate the observations. From these results, we conclude that parameter ν can be accurately recovered by the current 4D-Var model.

3.2.2. Thermal diffusivity recovery. Assume that the initial velocity and temperature fields and the viscosity profile are known for diffusivity profile recovery. Since different observations lead to the same conclusion, we present only the case 4 result, which uses observation set B. Figure 5 shows diffusivity profiles recovered at different iterations. It is of interest to observe that the thermal diffusivity profile can be recovered from radial velocity information. This demonstrates the coupling

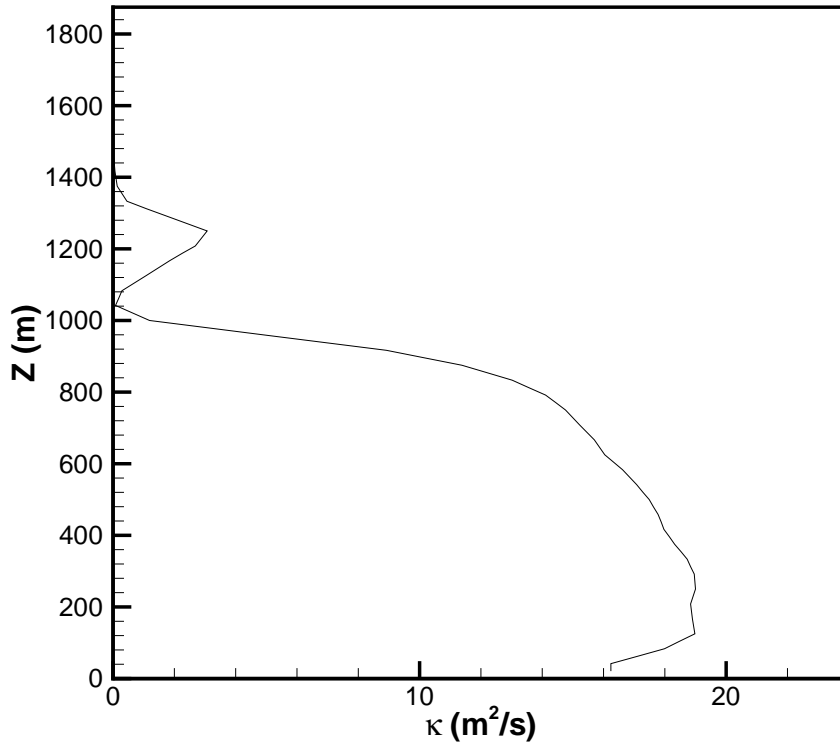


FIG. 4. Thermal diffusivity profile used to generate observation set A.

of temperature and velocity fields and that some thermodynamic parameters can be estimated from wind information.

3.2.3. Eddy viscosity and thermal diffusivity recovery. In cases 5, 6, and 7, both eddy viscosity and thermal diffusivity are treated as control variables. Cases 5 and 7 use the initial profiles shown in Figure 6(1a). Case 6 uses the initial profiles shown in Figure 6(2a), where $\nu(z)$ and $\kappa(z)$ have maximum values at the surface and decrease linearly with height until reaching the inversion layer. Recovered profiles for cases 5 and 6 are shown in Figures 6(1b) and 6(2b). Viscosity profiles can be fully recovered from both initial guesses only after 10 iterations; however, diffusivity profiles are only partially recovered after 50 iterations. With more iterations, the recovered diffusivity profile improves, but slowly, toward the exact profile for both cases. We draw two conclusions from these results. First, both $\nu(z)$ and $\kappa(z)$ profiles can be recovered simultaneously from the radial velocity field. Second, the recovery of profiles $\nu(z)$ and $\kappa(z)$ are not sensitive to initial guesses.

The question remains, Why do these cases take so many more iterations to fully recover κ profiles compared to case 4, which takes about 45 iterations (Figure 5)? It was expected that if the ν profiles in cases 5 and 6 could be fully recovered in about 10 iterations, as in case 2, which recovers ν alone, the κ profiles should have been

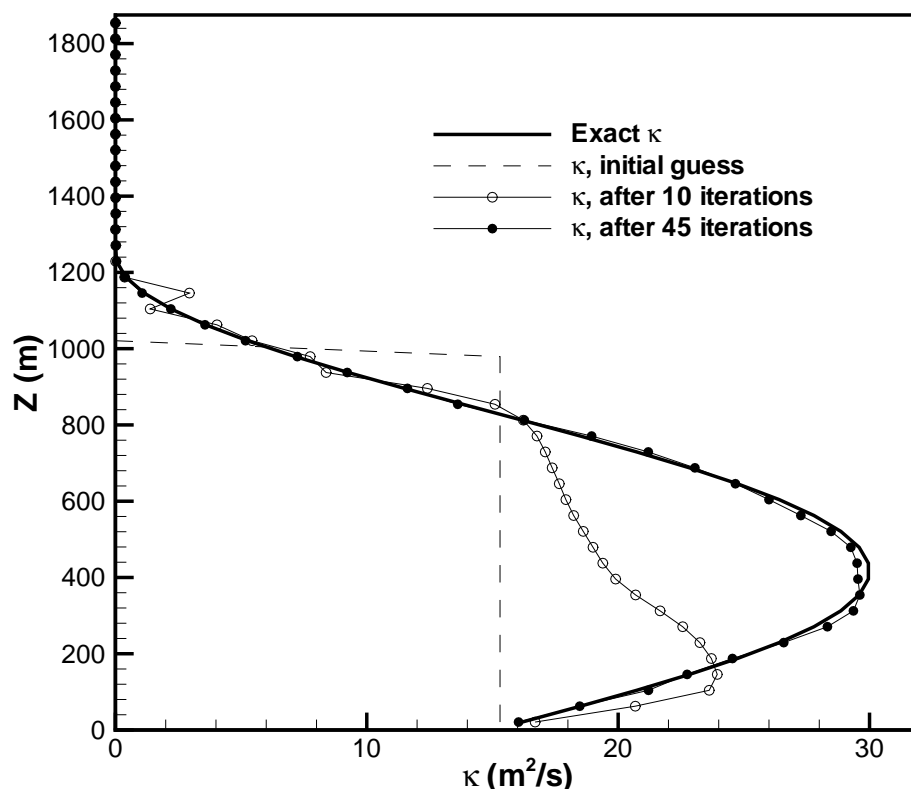


FIG. 5. Comparison of the recovered thermal diffusivity with the exact profile for case 4.

recovered in about 40 more iterations, as in case 4, which recovers κ alone. In fact, more than 100 iterations are required to recover the κ profiles. Recovery of the κ profiles is extremely slow. Two 1D cross sections of cost function shown in Figure 7 reveal that the cost function is much more sensitive to eddy viscosity than thermal diffusivity. The averaged magnitude of $\nabla_{\nu}H$ is more than 100 times that of $\nabla_{\kappa}H$. This suggests that the search directions for the optimal solutions in cases 5 and 6 are more dependent on the gradient information $\nabla_{\nu}H$ than on $\nabla_{\kappa}H$.

Linear transformation of control variables, namely rescaling control variables, could affect the convergence property of the minimization. Use of $(\nu(z), \kappa(z)/2)$ or $(\nu(z), \kappa(z)/3)$ as control variables does produce much better results than cases 5 and 6, which do not use rescaling. Figure 8 shows recovered profiles after 10 and 50 iterations for case 7, in which a scaling factor of $1/2$ is applied. The results suggest that proper rescaling is important for minimization performance (see [2, 31]). We use the perturbation method to approximate the second derivatives of the cost function with the central difference scheme. The Hessian matrices at the exact solution points are obtained for selected cases. Following the similar approach as in [36], we calculate maximum and minimum eigenvalues of the Hessian and the condition numbers using the power method and the inverse power method [5]. Results are listed in Table 2. The

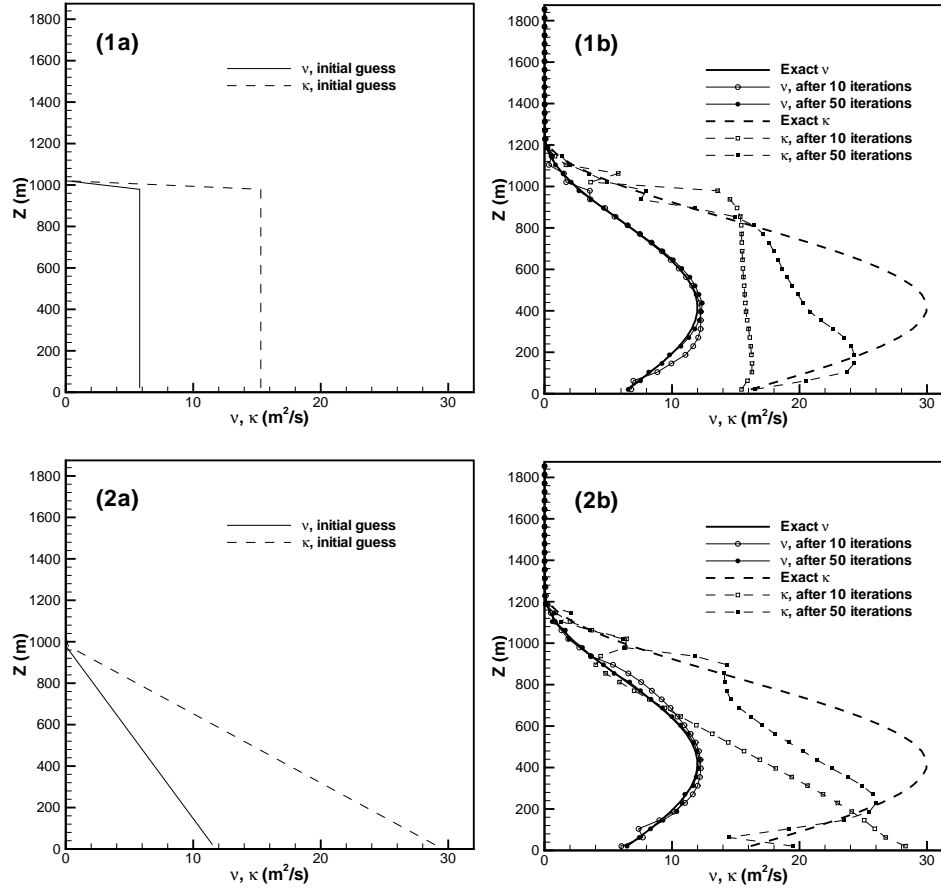


FIG. 6. Initial guesses (1a, 2a) and recovered profiles (1b, 2b) for cases 5 and 6.

condition number of the Hessian for case 4 is more than 10 times larger than that for case 2, thus substantially reducing the convergence speed for case 4. When both $\nu(z)$ and $\kappa(z)$ are control variables, as in cases 5 and 6, the condition number is increased by a factor of 30.5, compared to case 4. The maximum and minimum eigenvalues for cases 5 and 6 seem to be correlated with the maximum eigenvalue of the Hessian for case 2 and the minimum eigenvalue of the Hessian for case 4, respectively. The simple rescaling method applied to case 7 effectively reduces the condition number by a factor of 4.0. The change of variable can be achieved through other means. For instance, the background error covariance matrix can be used to perform the variable change in the adjoint model [4]. The change of variable can also be replaced with sophisticated preconditioning algorithms (e.g., [39, 40]) for better convergence. Nevertheless, the current simple rescaling improves the minimization performance, as can be seen in Figures 9 and 10. Therefore, all the ITEs in the next section use a scaling factor of 1/2 for thermal diffusivity retrieval.

4. Flow field retrieval. The foregoing experiments prove that the adjoint model can recover the parameters. It is not, however, realistic to assume initial

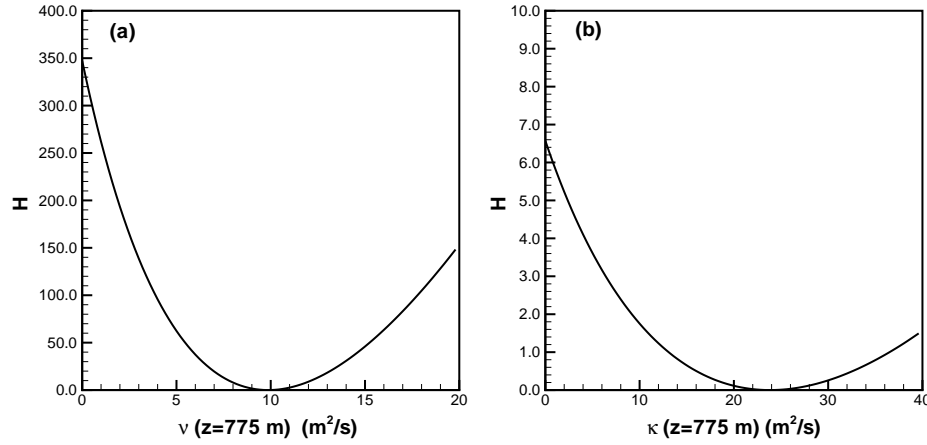


FIG. 7. Two 1D cross sections of cost function H in cases 5 and 6. Other dimensions of the 90-dimensional parameter set are fixed as the exact values.

velocity and temperature as known variables for 4D-Var. Therefore, initial conditions must be included as control variables. In this section, all the ITEs include the initial flow fields U , V , W , and θ at every grid point as control variables. This could be problematic as the number of control variables increases from $2N_z$ (including both ν and κ profiles) to $2N_z + 4N_x \times N_y \times N_z$. Thus, this section aims to answer two questions. First, is it possible to recover all control variables? Second, will parameter retrieval improve retrieval data quality? Observation set B is used for the ITEs listed in Tables 3 and 4. To measure the quality of the retrieved data, we calculate root-mean-square (RMS) errors ϵ_f and correlation coefficients γ_f between the retrieved variables and the exact counterparts. The correlation coefficient is defined as

$$(4.1) \quad \gamma_f = \frac{\overline{f \cdot f_o}}{\sqrt{\overline{f^2}} \cdot \sqrt{\overline{f_o^2}}},$$

where f designates any fluctuating velocity component or temperature of the retrieved field, and f_o represents its exact counterpart. The overline denotes spatial averaging in an x - y plane. ϵ_f and γ_f can be calculated at each time step and every vertical level for each variable. RMS errors and correlation coefficients listed in Table 4 are averaged over vertical levels below the capping layer, i.e., $z < z_i$, where turbulence is active. These quantities are computed using data at the middle of the assimilation time window (150 sec), where the best results are obtained (see [10]).

Compared with case 7 discussed in section 3.2, case 8 adds the initial flow and temperature fields as control variables. The convergence criterion of (3.4) is applied. The maximum iteration number is raised from 50 to 100 due to the large number of control variables. 13 volumes of radial velocity data are used. The recovered ν profile is in excellent agreement with the exact profile. The κ profile is only partially recovered. Later, we will see the recovered ν and κ profiles from a case using much fewer observations (three volumes). From Table 4, correlation coefficients of velocity components U , V , and W at $t = 150$ sec are 0.988, 0.987, and 0.979. For

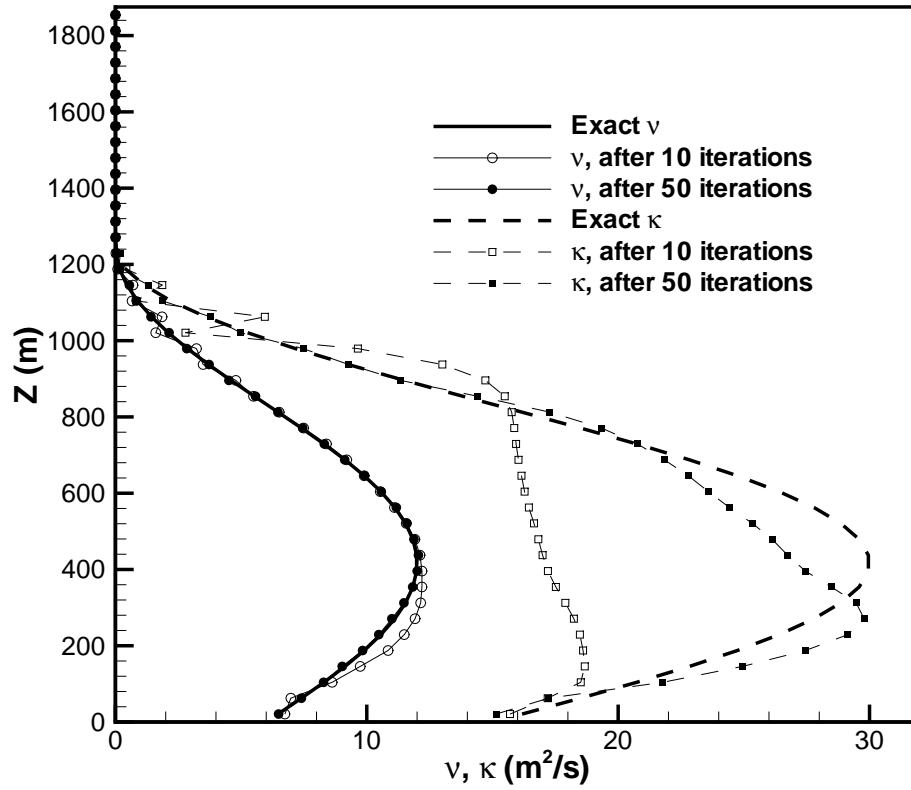


FIG. 8. Comparison of recovered eddy viscosity and thermal diffusivity with the exact profiles for case 7.

TABLE 2

Maximum and minimum eigenvalues and condition numbers of the Hessian matrices at the exact solution points for selected cases using the power method and the inverse power method.

Case	Maximum eigenvalue	Minimum eigenvalue	Condition number
2	$7.058 \cdot 10^2$	$3.862 \cdot 10^{-1}$	$1.828 \cdot 10^3$
4	$9.241 \cdot 10^1$	$4.226 \cdot 10^{-3}$	$2.187 \cdot 10^4$
5, 6	$7.059 \cdot 10^2$	$1.058 \cdot 10^{-3}$	$6.675 \cdot 10^5$
7	$7.064 \cdot 10^2$	$4.226 \cdot 10^{-3}$	$1.672 \cdot 10^5$

temperature it is 0.841. The averaged RMS errors for all three velocity components and temperature are 0.137 m/s, 0.158 m/s, 0.163 m/s, and 0.181 K. Considering the maximum velocity in the whole domain at approximately 10 m/s, the relatively small RMS errors demonstrate excellent agreement between retrieved variables and exact counterparts. The agreement also reflects on high values of correlation coefficients. The retrieved temperature data are not as good as the velocity field. $\gamma_\theta = 0.841$, however, still indicates a reasonably good retrieval. From case 8, we see that 4D-Var with the control space comprising both distributed initial field and model parameters works well and recovers the ν profile with moderate computational cost. This answers

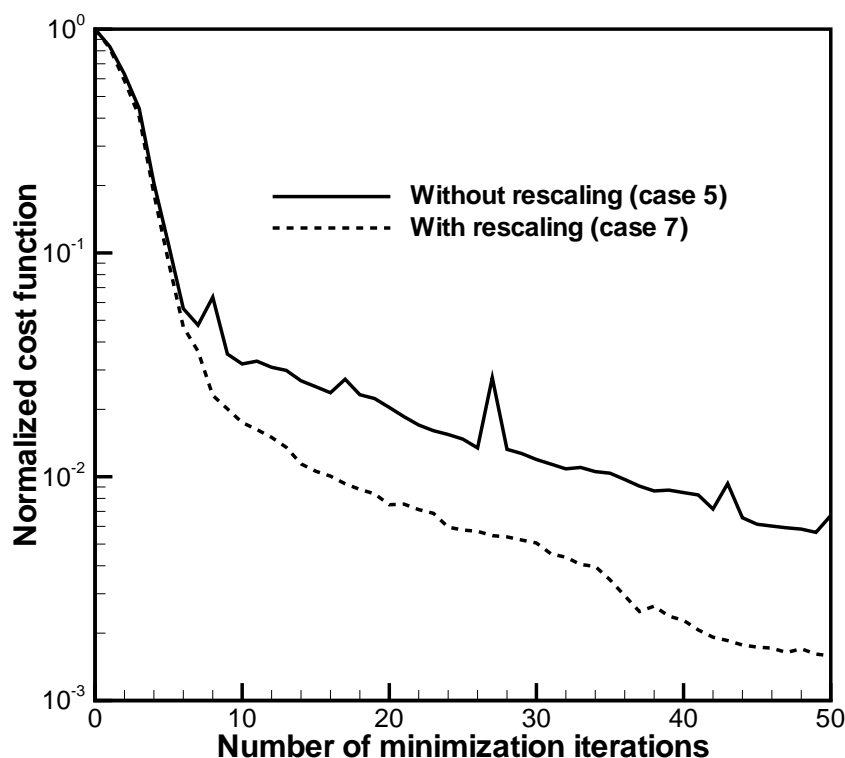


FIG. 9. Evolution of cost function as a function of minimization iteration number.

our first question.

One question remains. Can the profile of ν , optimized through 4D-Var, improve retrieval quality? To answer this question, we shall compare case 8 with cases 9, 10, and 11, which use fixed ν and κ profiles. In case 9, the profiles are fixed as those of initial guesses for case 8, shown in Figure 3(d). The profiles for case 10 are the same as those shown in Figure 3(a) and Figure 4, used in generating observation set A. Case 11 uses the same profiles as in creating observation set C. Except for the ν and κ profiles, cases 8, 9, 10, and 11 have exactly the same conditions. Correlation coefficients and RMS errors (Table 4) indicate that case 8 yields the best result of the four and case 11 gives the worst result. Retrieved data are examined for different vertical levels. Figure 11 shows vertical distribution of RMS errors. Errors of retrieved velocity components in case 11 are almost doubled compared to the other three cases at lower levels. At higher levels, RMS errors of retrieved temperature from case 9 are much larger than other cases. The results of cases 8 and 10 are similar, though case 8 has smaller RMS errors than case 10 for all variables at all levels. The difference between cases 8 and 10 (Figure 11) implies that the effect of inaccurate parameterization can be felt throughout the domain. These results clearly demonstrate that the 4D-Var method that optimizes ν and κ values improves retrieval quality. At least it does not

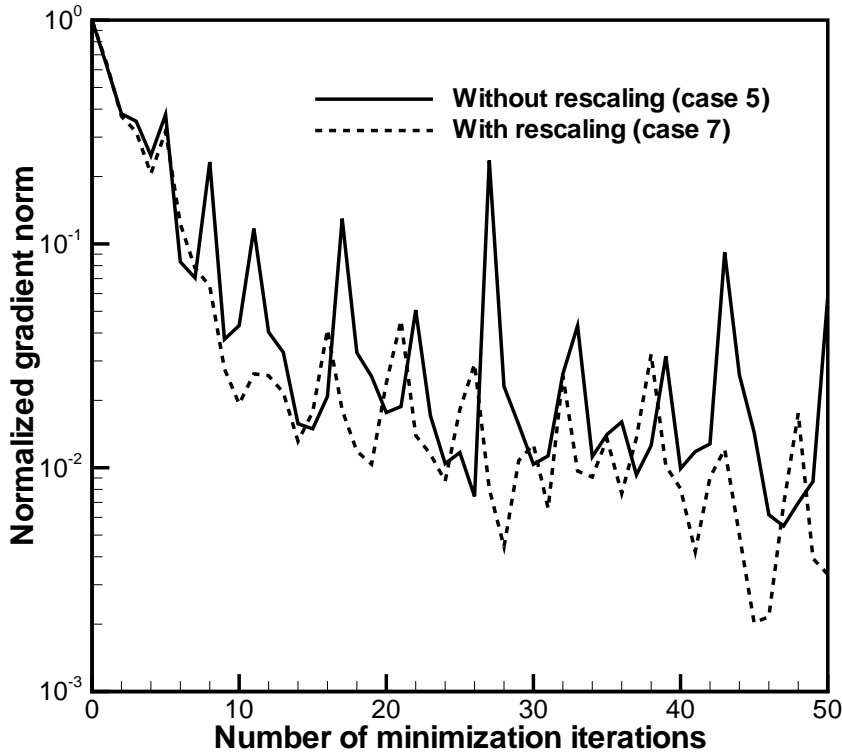


FIG. 10. Evolution of gradient norm as a function of minimization iteration number.

degrade the retrieval.

Since observational errors are inevitable in real field measurement, uniformly distributed random errors ranging from -0.5 to 0.5 m/s are added for case 12 to the radial velocity field. The results (Table 4) show correlation coefficients γ_u , γ_v , and γ_w for case 12 of 0.974, 0.975, and 0.951, respectively. RMS errors of the retrieved velocity components are 0.200 m/s, 0.218 m/s, and 0.255 m/s. As expected, retrieved temperature is not as good as retrieved velocity, with correlation coefficient $\gamma_\theta = 0.813$ and RMS error $\epsilon_\theta = 0.206$ K. Overall, retrieved data are quite satisfactory even in the presence of observational errors.

It is impossible to acquire 13 volumes of radial velocity data in five minutes using current lidar technology; we therefore reduce the observations to three volumes. To emulate the scanning feature of lidar, only several horizontal planes of data are made available at each instant. Cases 13–17 are intended to repeat cases 8–12 but with only three volumes of data. Case 14, using initial guesses as fixed parameter profiles, fails to generate retrieval flow fields due to instability in the forward integration after eight iterations. The sudden change of parameters at the capping layer is speculated to cause the instability. Retrieval results from other cases are consistent with those from cases 8–11. Case 15, which optimizes ν and κ profiles, results in better retrieval than

TABLE 3

Descriptions of ITEs presented in section 4. In cases 12 and 17, uniformly distributed random error $|\epsilon| < 0.5$ m/s is added to the radial velocity data.

Case	Volumes of observations	$\nu(z)$ and $\kappa(z)$
8	13	treated as control variables
9	13	fixed as those of initial guesses
10	13	fixed as those of observation set A
11	13	fixed as those of observation set C
12	13	treated as control variables
13	3	treated as control variables
14	3	fixed as those of initial guesses
15	3	fixed as those of observation set A
16	3	fixed as those of observation set C
17	3	treated as control variables
18	2	treated as control variables

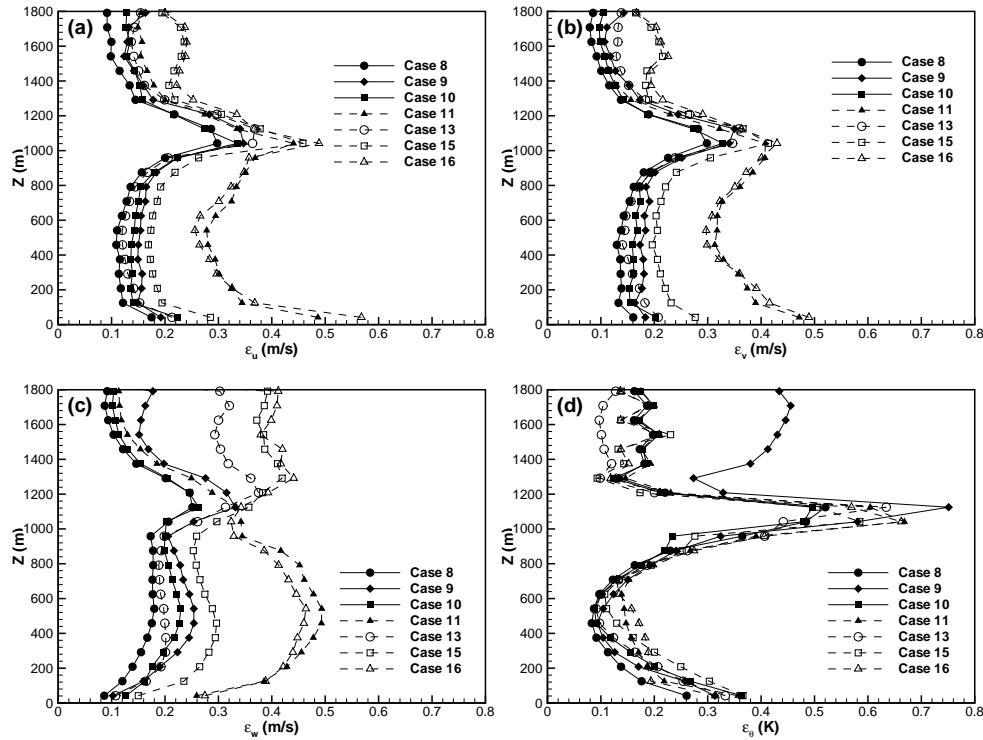
TABLE 4

Results of ITEs presented in section 4. Case 14 stops after eight iterations due to instability in the forward flow simulation. For cases 11, 16, and 17, cost function H levels out after 42, 39, and 70 iterations, respectively. For other cases, the results after 100 iterations are shown. ϵ_u , ϵ_v , and ϵ_w are in a unit of m/s. ϵ_θ is in K .

Case	γ_u	γ_v	γ_w	γ_θ	ϵ_u	ϵ_v	ϵ_w	ϵ_θ
8	0.988	0.987	0.979	0.841	0.137	0.158	0.163	0.181
9	0.981	0.980	0.966	0.782	0.168	0.190	0.220	0.200
10	0.983	0.983	0.971	0.803	0.163	0.180	0.202	0.194
11	0.931	0.931	0.882	0.718	0.329	0.360	0.436	0.235
12	0.974	0.975	0.951	0.813	0.200	0.218	0.255	0.206
13	0.986	0.984	0.971	0.820	0.151	0.175	0.190	0.220
15	0.974	0.972	0.949	0.764	0.202	0.230	0.266	0.222
16	0.935	0.934	0.890	0.716	0.326	0.359	0.414	0.234
17	0.939	0.941	0.895	0.740	0.309	0.336	0.405	0.269
18	0.965	0.962	0.928	0.758	0.241	0.279	0.325	0.234

cases that use fixed profiles. With random errors introduced into the observations, retrieval is still reasonably good. An interesting feature is seen in Figure 11. With optimized ν and κ parameters, case 13, which uses three volumes of data, obtains almost the same results as case 11, which uses 13 volumes of data and fixed ν and κ profiles.

When control variables only include eddy viscosity and thermal diffusivity in section 3, the ratio of observations to control variables is at least 3.456×10^3 (for three volumes of observations). After adding initial conditions as control variables, the ratio is reduced to 0.9995 for three volumes of observations. From a mathematical point of view, it is a marginally ill-posed problem, but the current 4D-Var system still manages to yield good results. To explain this, we need to look at the minimization method implemented. As a quasi-Newton method, L-BFGS approximates the Hessian matrix rather than computing it exactly. The updating formulation (see [12]) ensures that the Hessian matrix is always a positive definite matrix. This guarantees that the line search can be carried out continuously. As a result, we always get a solution even when the number of observations is close to the number of control variables. In those cases, some controls are not active in determining the cost function and may not have unique solutions. But the undetermined part of the solution will not compromise the process since it usually has little effect on flow history. This argument

FIG. 11. Vertical distributions of RMS errors at $t = 150$ sec.

might not be true for real observations, which are no longer perfectly consistent with the prediction model. The impact of incomplete observations was also discussed by Zou, Navon, and Le Dimet [36] using the shallow-water equations model. They found that the minimization is more sensitive to the availability of observations in space than in time. Thus, even when the observations are available at only two time steps of the assimilation window, a satisfactory retrieval can be reached. When the observations become severely scarce, proper penalization may be necessary to improve the conditioning of the minimization [11, 30, 36].

In case 18, the number of volumes of observations is further reduced to 2. Figure 12 shows the retrieved viscosity and diffusivity profiles. The viscosity profile is almost recovered, as is the diffusivity profile. Comparing the retrieved instantaneous velocity field in Figures 13 and 14, we see that microscale flow structures, such as convergence lines (updraft motions) and divergence regions (downdraft motions), are recovered in great detail.

It is well known that identifying spatially dependent parameters is often ill-posed and successful numerical techniques are always difficult to develop [17]. It lacks proof that our estimated parameter solution is unique, but the current method provides well-behaved results. Since the eddy viscosity parameters are model parameters rather than real physical parameters like molecular viscosity [29], we are more interested in improving retrieval of flow fields than identifying model parameters. The insensitivity of retrieval results to the addition of random errors indicates that the retrieval depends continuously on the observations. If observational errors are severe, Tikhonov

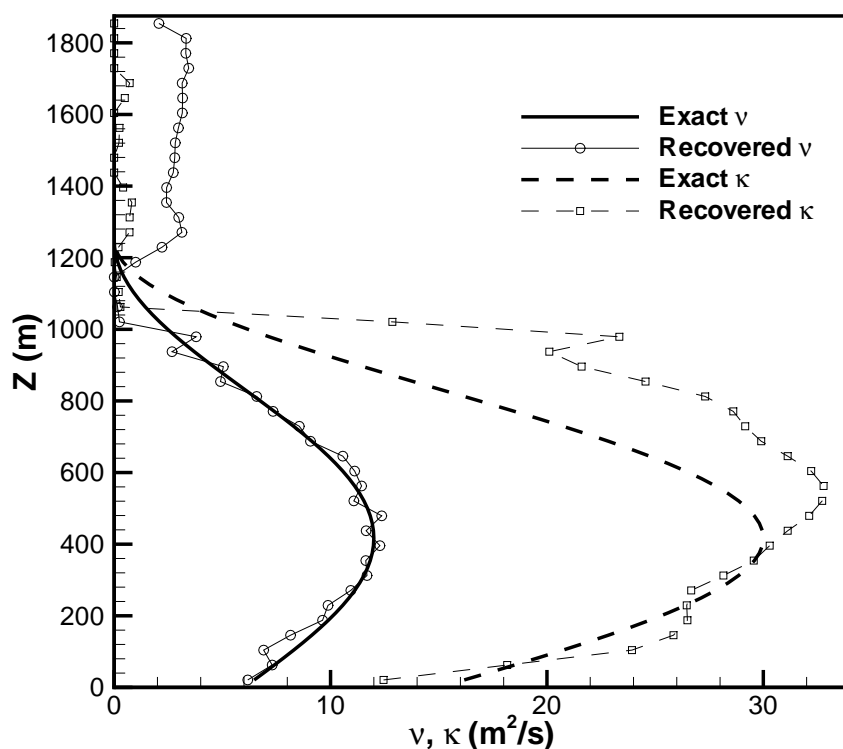


FIG. 12. Comparison of recovered eddy viscosity and thermal diffusivity with the exact profiles for case 18.

regularization (see [14, 17]) is suggested for generating smooth results.

5. Conclusions. We have proposed a method to optimize the profiles of eddy viscosity and thermal diffusivity using the 4D-Var adjoint model. Two sets of ITEs are conducted. One set aims to retrieve viscosity and/or diffusivity profiles alone by assuming known initial conditions. Results show that the eddy viscosity profiles can be recovered effectively, while the recovery of thermal diffusivity profiles takes more iterations. Rescaling thermal diffusivity is found to speed up the minimization process using the L-BFGS quasi-Newton method. The second set of ITEs retrieves both initial velocity and temperature fields and profiles of viscosity and diffusivity simultaneously. Despite of the dramatic increase of control variables, the proposed method works well. The retrieval quality improves as compared with the previous approach, which prescribes the model parameters. The new method is further tested by adding observational errors and reducing available observations. Results indicate that the method still retrieves velocity and temperature fields. In general, the quality of retrieved velocity is better than that of temperature, since radial velocity is the only kind of observation. Lack of temperature information degrades the retrieved temperature field more than the velocity field. For this reason, diffusivity profile

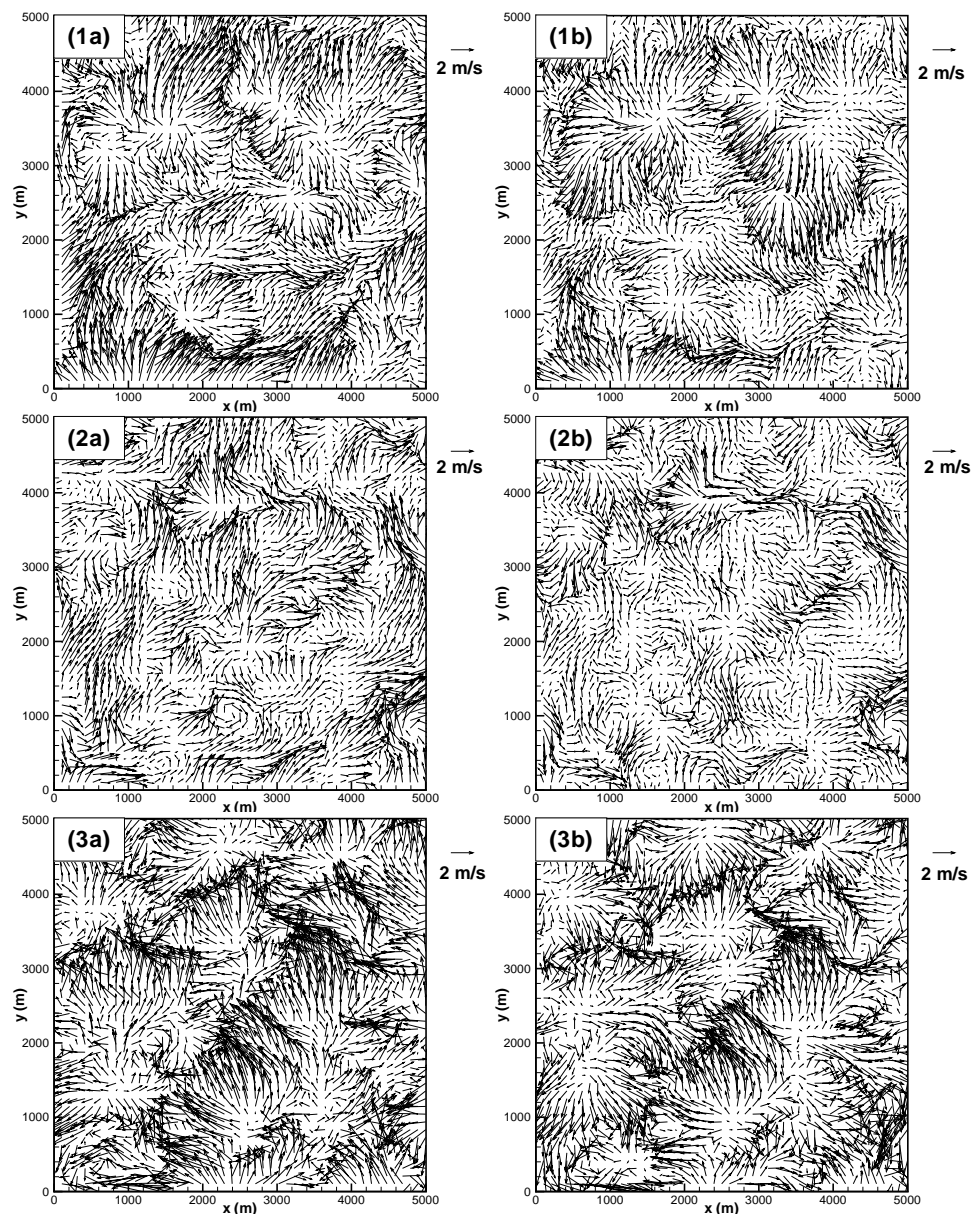


FIG. 13. Comparison of retrieved and exact flow fields at $t = 150$ sec for case 18. Horizontal fluctuating velocity vectors are shown. $z = (1) 895.8\text{m}, (2) 480.0\text{m}, (3) 62.5\text{m}$. (a) Retrieved velocity field; (b) exact velocity field.

recovery is not as good as viscosity profile recovery.

There are limits to the variational data assimilation, which assumes the model being perfect. As only the synthetic observations generated by the prediction model are currently used, it is necessary to further test the method using real data in the future. The success of 4D-Var, to a large extent, relies on the accuracy of the physical model chosen to describe the ABL flow. Although our current approach allows a greater

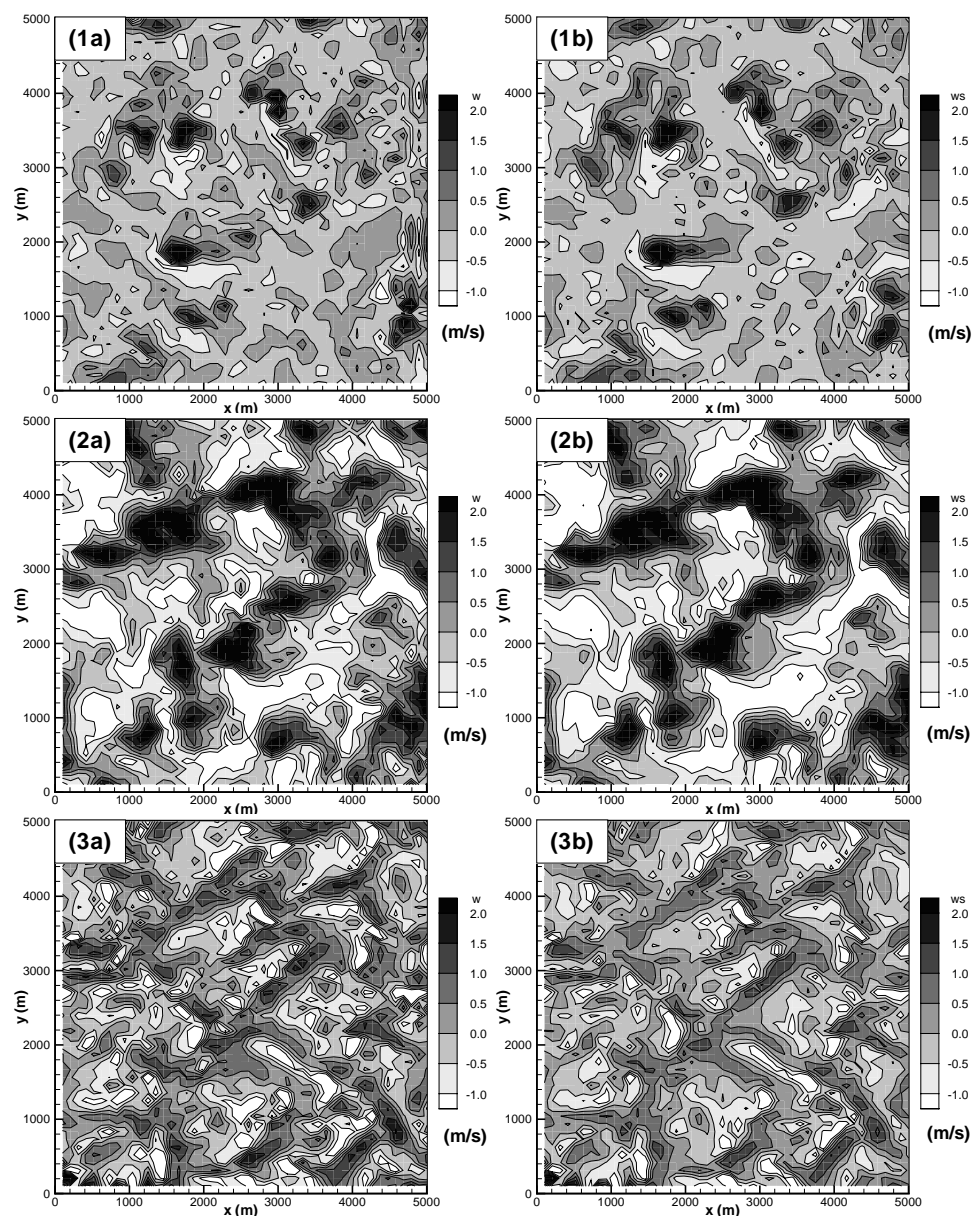


FIG. 14. Comparison of retrieved and exact flow fields at $t = 150$ sec for case 18. Contours of vertical fluctuating velocity are shown. $z = (1) 895.8\text{m}$, $(2) 480.0\text{m}$, $(3) 62.5\text{m}$. (a) Retrieved velocity field; (b) exact velocity field.

degree of freedom in SGS parameterization by treating model parameters as control variables, imperfect model prediction could eventually deviate from true atmospheric state. Zhu and Navon [35] demonstrated that the optimally identified parameters give a positive impact on the ensuing forecasts. Using the FSU Global Spectral Model, they showed that the model loses the impact of optimal initial conditions first, while the effect of optimized parameters persists a longer time. Furthermore, the retrieval

quality is limited by the observational quality. Both velocity and space resolutions set limitations on 4D-Var retrieval results. While 4D-Var can not only recover cross-beam velocity components but also fill gaps in observational fields, it cannot retrieve high resolution results from a sparse observational set with large observational errors.

Acknowledgments. We thank the National Partnership for Advanced Computational Infrastructure, sponsored by the National Science Foundation, for the computing time used in the research of this paper.

REFERENCES

- [1] T. CHAI, *Four-Dimensional Variational Data Assimilation Using Lidar Data*, Ph.D. dissertation, University of Iowa, Iowa City, IA, 2002.
- [2] W. CHAO AND L.-P. CHANG, *Development of a four-dimensional variational analysis system using the adjoint method at GLA. Part 1: Dynamics*, Mon. Wea. Rev., 120 (1993), pp. 1661–1673.
- [3] D. I. COOPER, W. E. EICHINGER, R. E. ECKE, J. C. Y. KAO, J. M. REISNER, AND L. L. TELLIER, *Initial investigation of microscale cellular convection in an equatorial marine atmospheric boundary layer revealed by lidar*, Geophys. Res. Lett., 24 (1997), pp. 45–48.
- [4] P. COURTIER, *Dual formulation of four-dimensional variational assimilation*, Q. J. R. Meteorol. Soc., 123 (1997), pp. 2449–2961.
- [5] H. G. GOLUB AND C. VAN LOAN, *Matrix Computations*, 2nd ed., Johns Hopkins Ser. Math. Sci. 3, The Johns Hopkins University Press, Baltimore, MD, 1989.
- [6] C. J. GRUND, R. M. BANTA, S. A. COHN, C. L. FRUSH, J. L. GEORGE, K. R. HEALY, J. N. HOWELL, S. D. MAYOR, R. A. RICHTER, AND A. M. WEICKMANN, *The high resolution Doppler lidar: A new tool for boundary layer research*, in Proceedings of the 12th Symposium on Boundary Layers and Turbulence, Vancouver, BC, Canada, 1997, pp. 15–16.
- [7] D. H. LENSCHOW, J. C. WYNGAARD, AND W. T. PENNELL *Mean-field and second-moment budgets in a baroclinic, convective boundary layer*, J. Atmospheric Sci., 37 (1980), pp. 1313–1326.
- [8] Y. LEREDDE, J.-M. LELLOUCHE, J.-L. DEVENON, AND I. DEKEYSER, *On initial, boundary conditions and viscosity coefficient control for Burgers' equation*, Internat. J. Numer. Methods Fluids, 28 (1998), pp. 113–128.
- [9] Y. LEREDDE, J.-L. DEVENON, AND I. DEKEYSER, *Turbulent viscosity optimized by data assimilation*, Ann. GeoPhysicae, 17 (1999), pp. 1463–1477.
- [10] C.-L. LIN, T. CHAI, AND J. SUN, *Retrieval of flow structures in a convective boundary layer using an adjoint model: Identical twin experiments and coherent structures in the convective planetary boundary layer*, J. Atmospheric Sci., 58 (2001), pp. 1767–1783.
- [11] C.-L. LIN, T. CHAI, AND J. SUN, *On the smoothness constraints for four-dimensional data assimilation*, J. Comput. Phys., 181 (2002), pp. 430–453.
- [12] D. C. LIU AND J. NORCEDAL, *On the limited memory BFGS method for large scale optimization*, Math. Programming, 45 (1989), pp. 503–528.
- [13] C.-H. MOENG, *A large-eddy-simulation model for the study of planetary boundary-layer turbulence*, J. Atmospheric Sci., 41 (1984), pp. 2052–2062.
- [14] V. A. MOROZOV AND M. STESSIN, *Regularization Methods for Ill-Posed Problems*, CRC Press, Boca Raton, FL, 1993.
- [15] S. G. NASH AND J. NORCEDAL, *A Numerical Study of the Limited Memory BFGS Method and the Truncated-Newton Method for Large Scale Optimization*, Tech. report NAM 02, Northwestern University, Evanston, IL, 1989.
- [16] I. M. NAVON, X. ZOU, J. DERBER, AND J. SELA, *Variational data assimilation with an adiabatic version of the NMC spectral model*, Mon. Wea. Rev., 113 (1992), pp. 2142–2157.
- [17] I. M. NAVON, *Practical and theoretical aspects of adjoint parameter estimation and identifiability in meteorology and oceanography*, Dynam. Atmos. Oceans, 27 (1998), pp. 55–79.
- [18] J. NOCEDAL AND S. J. WRIGHT, *Numerical Optimization*, Springer, New York, 1999.
- [19] V. G. PANCHANG AND J. E. RICHARDSON, *Inverse adjoint estimation of eddy viscosity for coastal flow models*, J. Hydraulic Eng., 119 (1993), pp. 506–525.
- [20] F. RABIER AND P. COURTIER, *Four-dimensional assimilation in the presence of baroclinic instability*, Q. J. R. Meteorol. Soc., 118 (1992), pp. 649–672.
- [21] R. B. STULL, *An Introduction to Boundary Layer Meteorology*, Kluwer Academic Publishers, Dordrecht, 1994.

- [22] P. P. SULLIVAN, J. C. MCWILLIAMS, AND C.-H. MOENG, *A subgrid-scale model for large-eddy simulation of planetary boundary-layer flows*, Boundary-Layer Meteorol., 71 (1994), pp. 247–276.
- [23] J. SUN, D. W. FLICKER, AND D. K. LILLY, *Recovery of three-dimensional wind and temperature fields from simulated single-Doppler radar data*, J. Atmospheric Sci., 48 (1991), pp. 876–890.
- [24] J. SUN AND A. CROOK, *Wind and thermodynamic retrieval from single-Doppler measurements of a gust front observed during Phoenix II*, Mon. Wea. Rev., 122 (1994), pp. 1075–1091.
- [25] J. SUN AND A. CROOK, *Comparison of thermodynamic retrieval by the adjoint method with the traditional retrieval method*, Mon. Wea. Rev., 124 (1996), pp. 308–324.
- [26] J. SUN AND A. CROOK, *Dynamical and microphysical retrieval from Doppler radar observations using a cloud model and its adjoint. Part II: Retrieval experiments of an observed Florida convective storm*, J. Atmospheric Sci., 55 (1998), pp. 835–852.
- [27] J. SUN AND A. CROOK, *Real-time low-level wind and temperature analysis using single WSR-88D Data*, Weather Forecasting, 16 (2001), pp. 117–132.
- [28] O. TALAGRAND AND P. COURTIER, *Variational assimilation of meteorological observations with the adjoint vorticity equation. I: Theory*, Q. J. R. Meteorol. Soc., 113 (1987), pp. 1311–1328.
- [29] T. TENNEKES AND J. L. LUMLEY, *A First Course in Turbulence*, MIT Press, Cambridge, MA, 1997.
- [30] W. C. THACKER, *Fitting models to inadequate data by enforcing spatial and temporal smoothness*, J. Geophys. Res., 93 (1988), pp. 10655–10665.
- [31] J. VERLINDE AND W. R. COTTON, *Fitting microphysical observations of nonsteady convective clouds to a numerical-model: An application of the adjoint technique of data assimilation to a kinetic model*, Mon. Wea. Rev., 121 (1993), pp. 2776–2793.
- [32] B. WU, J. VERLINDE, AND J. SUN, *Dynamical and microphysical retrieval from Doppler radar observations of a deep convective cloud*, J. Atmospheric Sci., 57 (2000), pp. 262–283.
- [33] L. YU AND J. J. O'BRIEN, *Variational estimation of the wind stress drag coefficient and the oceanic eddy viscosity profile*, J. Phys. Oceanogr., 21 (1991), pp. 709–719.
- [34] K. ZHU, I. M. NAVON, AND X. ZOU, *Variational data assimilation with a variable resolution finite-element shallow-water equations model*, Mon. Wea. Rev., 122 (1994), pp. 946–965.
- [35] Y. Q. ZHU AND I. M. NAVON, *Impact of parameter estimation on the performance of the FSU Global Spectral Model using its full physics adjoint*, Mon. Wea. Rev., 127 (1999), pp. 1497–1517.
- [36] X. ZOU, I. M. NAVON, AND F. X. LE DIMET, *Incomplete observations and control of gravity waves in variational data assimilation*, Tellus, 44A (1992), pp. 273–296.
- [37] X. ZOU, I. M. NAVON, AND J. G. SELA, *Variational data assimilation with moist threshold processes using the NMC spectral model*, Tellus, 45A (1993), pp. 370–387.
- [38] X. ZOU, I. M. NAVON, M. BERGER, K. H. PHUA, T. SCHLICK, AND F. X. LE DIMET, *Numerical experience with limited-memory quasi-Newton and truncated Newton methods*, SIAM J. Optim., 3 (1993), pp. 582–608.
- [39] M. ZUPANSKI, *A preconditioning algorithm for large-scale minimization problems*, Tellus, 45A (1993), pp. 478–492.
- [40] M. ZUPANSKI, *A preconditioning algorithm for four-dimensional variational data assimilation*, Mon. Wea. Rev., 124 (1996), pp. 2562–2573.